Journal of Materials Chemistry A

ROYAL SOCIETY OF CHEMISTRY

PAPER

View Article Online
View Journal | View Issue

Cite this: J. Mater. Chem. A, 2025, 13, 2974

Safe and stable Zn-lignin batteries with a biopolymer based hydrogel electrolyte†

Ujwala Ail,*[a] Jakob Backe,[b] Zia Ullah Khan,[a] Rui Shu,[a] Jaywant Phopase,[a] Magnus Berggren[c] and Reverant Crispin *[ac]

The safety risks associated with organic solvent-based batteries for stationary energy storage have driven scientists to reconsider aqueous electrolytes combined with ultra low-cost materials. In this context, zinc (Zn) metal and biopolymer lignin are certainly among the most abundant and economical electroactive materials on Earth, displaying compatibility in their redox activity to fit the stability window of aqueous electrolytes. But, up to now, the electrolyte solutions in those systems incorporate fluorinated organic salts or bio-ionic liquids, both of which are detrimental to the environment and expensive. In this work we use a state-of-the-art lignin electrode based on catechol functionalized lignin (LC) nano-composited with carbon black (C) and a biopolymer hydrogel electrolyte based on agarose with non-fluorinated Zn salt. The optimization of the hydrogel's composition was realized by reducing the amount of free water by promoting its bonding with additional glycerol. The hydrogel facilitates the growth of Zn in the (002) plane, preventing dendritic formation. The highest discharge capacity of 79.7 mA h g_{LC}^{-1} was obtained at 0.05 A g^{-1} charge/discharge rate for the buffered 3% agarose hydrogel electrolyte containing 25% glycerol with 1 M Zn^{2+}. The hydrogel containing 25% glycerol with 1 M Zn^{2+} and 1 M K^{+} in the absence of buffering shows the best cycle performance with 78% capacity retention after 26 000 cycles at 1 A g^{-1} with a capacity of 58 mA h g_{LC}^{-1} at 0.05 A g^{-1}. This study shows the possibility of a safe, affordable, bio-based environmentally friendly energy storage system that has the potential for large-scale applications.

Received 10th October 2024
Accepted 5th December 2024

DOI: 10.1039/d4ta07213h

rsc.li/materials-a

1. Introduction

The growing impact of climate change, driven by the extensive reliance on fossil fuels, is pushing nations to pivot towards indigenous renewable energy sources such as solar and wind for their electricity needs. In this crucial transition, battery storage systems are set to play a crucial role. Despite the vast amount of research aimed at developing batteries capable of storing sustainable energy, it is imperative that the batteries themselves embody sustainability. The precarious supply chain for scarce battery-grade materials, like those found in lithium-ion batteries (LIBs), coupled with the safety concerns related to their organic electrolytes, renders these batteries impractical for widespread use, especially within the stationary energy storage sector. From this standpoint, it becomes vital to explore sustainable, rechargeable battery technologies and to develop high-performance, cost-effective battery electrodes through environmentally friendly methods, to bolster our collective efforts against climate change.

Zn-ion batteries (ZIBs) are one such major alternative in terms of both performance and manufacturing compatibility to compete alongside LIBs for stationary batteries. Additionally, ZIBs use raw materials that are orders of magnitude more abundant than in a standard LIB.[1] Unlike the flammable electrolytes used in LIBs, Zn-ion technology uses water-based chemistry and hence is safer. This is the key feature that makes ZIBs especially attractive for residential energy storage. The low cost of Zn (~2.2 Euro per kg) that serves as an anode together with its high theoretical capacity of 820 mA h g^{-1} [2,3] results in a low-capacity cost of ~0.003 Euro per A h.

In the search for low-cost sustainable cathode materials, lignin, a byproduct of the large paper industry, has been proposed as a candidate for large-scale batteries. Lignin is an aromatic biopolymer and one of the cheapest organic materials (~0.6 Euro per kg) with electrochemical activity. As an insulator, lignin must be combined with an electronic conductor to form nanocomposites that can store electricity. The expected capacity of such a lignin–conductor nanocomposite is 80 mA h g^{-1},[4] which also makes lignin a low-cost battery material at ~0.008 Euro per A h. Lignin in the form of kraft lignin and lignosulfonate has been composited with conducting polymers[4–7] and carbon nanostructures.[8–13] Recently, we reported[14] the

[a]Laboratory of Organic Electronics (LOE), Department of Technology and Natural Sciences (ITN), Linköping University, Norrköping SE-601 74, Sweden. E-mail: reverant.crispin@liu.se; ujwala.ail@liu.se

[b]Ligna Energy AB, Källvindsgatan 5, Norrköping 60240, Sweden

[c]Wallenberg Wood Science Center, Department of Science and Technology (ITN), Linköping University, Norrköping SE-60174, Sweden

† Electronic supplementary information (ESI) available. See DOI: https://doi.org/10.1039/d4ta07213h

modification of kraft lignin (KL) by covalently attaching catechol molecules (termed lignocatechol, LC), which resulted in a 3 times increase in capacity up to 106 mA h g^{-1}.

Hence, both lignin and Zn are among the cheapest electroactive materials on the planet, while being non-toxic and easily recyclable. Zn–lignin batteries thus appear to be an attractive candidate for large- scale stationary batteries with very few reports so far. In the first work, lignosulfonate was composited with polypyrrole to form the cathode. Zn acetate (in an ionic liquid, choline acetate and water) was the electrolyte, but the Zn–lignin battery displayed poor cyclic stability.[15] Recently, $Zn(TFSI)_2$ in "water-in-polyelectrolyte" has been proposed as a potentially stable electrolyte for use with a lignin–carbon electrode[16] and a Zn–lignin battery was demonstrated to undergo 8000 cycles at 1 A g^{-1} using this electrolyte.[17] Synthetic polycatechol has been used as the cathode in a ZIB with a $Zn(TFSI)_2$ aqueous electrolyte, demonstrating high cyclability over 48 000 cycles at a 30C rate.[18] These few early concepts use high-cost fluorinated salts, which move the concept away from the low-cost, sustainable, and safety related criteria for large-scale implementation. More importantly, the TFSI anion belongs to the per- and polyfluoroalkyl substances (PFAS) class of materials.[19] Due to the growing concerns regarding their environmental and health impacts, a stringent stance on these fluorinated compounds is observed globally.[19] Hence, to engineer an optimal Zn–lignin battery, it is imperative to identify an electrolyte that not only addresses the challenges associated with ZIBs (Fig. 1a), such as dendritic growth and the hydrogen evolution reaction at the Zn anode,[2,3,20–22] but also enhances the electroactivity of the lignin electrode.[16]

In ZIBs, Zn is deposited (also referred to as Zn plating) at the negative electrode (anode) during the charging process (−0.76 V *vs.* standard hydrogen electrode) and dissolved (also referred to as Zn stripping) during discharging (Fig. 1b). Hydrogen evolution is one of the major side reactions that occur simultaneously during Zn deposition in aqueous media. In aqueous electrolytes, Zn deposition takes place when potential is less than −0.15 V (*vs.* Zn^{2+}/Zn), which is beyond the electrochemical stability window of −0.05 to 1.7 V (*vs.* Zn^{2+}/Zn) water.[23–25] Hence, instead of utilizing the charge provided by the external circuit at the Zn electrode for Zn deposition (reduction), part of the charge is taken up by the unwanted hydrogen evolution reaction (HER) to form H_2 bubbles, which in turn can block the surface availability for Zn deposition. In addition, the consumption of protons in the HER results in a local increase in pH due to the formation of OH^- anions near to the Zn metal surface. This effect favors the Zn corrosion leading to the formation of $Zn(OH)_2$ or ZnO that can passivate the Zn surface resulting in a slow rate of oxidation (stripping).[21,24,25] These side reactions are correlated to the free water available in the electrolyte at the Zn anode.[21,24,26] Another issue is the dendritic growth of Zn, which happens when the Zn^{2+} ions transfer to the anode (Zn) surface under the combined influence of an uneven electric field and a concentration gradient during the initial plating process, subsequently gaining electrons and forming Zn atom nuclei.[27]

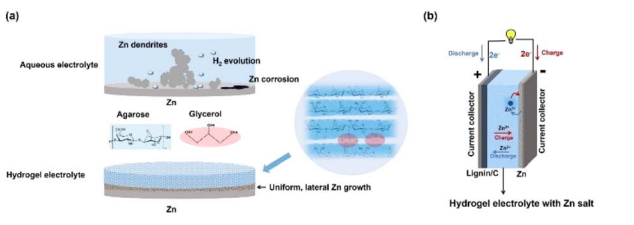

Fig. 1 (a) Schematic representation showing Zn deposition in aqueous and in hydrogel electrolyte and (b) basic configuration of a Zn-ion pseudocapacitive device with a lignin/C cathode and hydrogel electrolyte.

Many strategies have been proposed to suppress dendrite formation and the HER.[24,27–33] Among these approaches, hydrogel electrolytes have demonstrated the ability to prevent dendritic growth. They are also interesting due to their high ionic conductivity, flexibility and low temperature stability.[32,34] Hydrogels are polymeric materials with 3D network structures comprising physically or chemically crosslinked polymer chains having mesoporous space with enclosed water.[33–35] Bio-based materials are advantageous for use in hydrogel electrolytes due to their cost-effectiveness, natural sourcing, biodegradability, *etc.*[36–40]

In this work, we demonstrate a Zn–lignin battery with outstanding performance, utilizing environmentally friendly, safe biopolymer based materials. The lignin electrode is a nanocomposite of carbon black (C) and lignin functionalized with catechol groups (LC). The Zn salt is based on methane sulfonate, which has a biogenic origin and is biodegradable.[41,42] The hydrogel matrix used to load the salt is the biopolymer agarose, a natural polysaccharide extracted from marine red algae.[40,43] In addition, glycerol, another non-toxic biomolecule, is especially investigated as an additive to the hydrogel.[44,45] Hydrogel electrolytes are complex systems as water molecules in them differ depending on the nature of their solvation shells. When a water molecule has only water as the nearest neighbor, it is called a free water molecule like in bulk water. Solvation water molecules are those that interact with the ions of the electrolytes, and bonded water molecules are the ones that interact with the polymer matrix of the hydrogel. Given that free water molecules are known to promote the HER side reaction, a strategy similar to anti-freezing techniques is proposed in this work: the addition of glycerol to reduce the number of free water molecules. The hydrogen bonds formed between polyols and water molecules are stronger than those between water molecules themselves, leading to a decrease in the concentration of free water. Crucially, the incorporation of glycerol in the agarose hydrogel is expected to maintain Zn cation transport while limiting the HER by reducing the free water content. To the best of our knowledge, this strategy has not been applied to ZIBs; the resulting Zn–lignin battery displays remarkably high cycle stability over 10 000 cycles, a low leakage current density of 2–13 μA cm^{-2}, and slow self-discharge performance retaining 63–72% of its cell voltage over 5 days.

2. Experimental

2.1. Modified lignin (LC)

Lignoboost kraft lignin (KL) from Valmet was used for catechol modification by covalently linking *ortho*-catechol under solvent

free conditions, using sulfuric acid as a catalyst. Details of the synthesis are presented in our recent communication.[14]

2.2. Composite positive electrode (cathode) preparation

The LC and carbon black (C) (1 : 1) composite was prepared *via* mechanical milling in a planetary mill, Retsch PM 100 using ZrO_2 milling media at 500 rpm speed for 120 min with a ball/powder ratio of ~10–20 under dry conditions and an ambient atmosphere. The carbon black used was ENSACO 360 G (IMERYS, with a BET surface area of 780 $m^2\ g^{-1}$ supplier value). After the components were mixed, the aqueous slurry was prepared using CMC-SBR (carboxymethyl cellulose/styrene butadiene rRubber) (6%) as the binder system. The slurry was coated with a wet thickness of 200–300 μm onto Ni foil that was pre-coated with colloidal carbon. The film was dried at 60 °C for 2 h and pressed using a Durston DRM 130 roller press. The pressed material was cut into coin cell electrode formats. Mass loading of the LC/C cathode was between 3 and 4 mg cm^{-2}.

2.3. Hydrogel electrolyte preparation

Agarose powder (Sigma Aldrich, low EEO) was added to water containing 1 M Zn salt, namely Zn mesylate (Zn salt of methane sulfonic acid). The concentration of agarose used was 3% (wt%). The solution was heated to 70–80 °C for the dissolution of agarose after which the gel was poured onto the Petri dish. The hydrogel thickness was maintained at 1 mm. The gel was allowed to cool to room temperature (RT) and the formed hydrogel was kept for 3 h at RT for drying. The solidified gel was cut into discs and used as electrolyte in the coin cell. Modifications to the agarose gel were carried out by replacing a portion of water with glycerol (0, 5, 10, 15, 20 and 25%). Above 25% glycerol, the hydrogel began to phase-separate and water droplets were formed on the surface of the hydrogel during drying at RT. Buffering (pH = ~5.5) of the hydrogel was carried out using 2-(*N*-morpholino) ethanesulfonic acid (MES) and potassium hydroxide. The hydrogel, in the absence of buffering, was found to have a pH of 4.9. Zn methane sulfonate salt was prepared by reacting methane sulfonic acid and Zn acetate and then purified through recrystallization. Potassium methane sulfonate (potassium mesylate) was purchased from Sigma Aldrich. Hydrogels are named based on the liquid state compositions.

2.4. Characterization

Differential scanning calorimetry (DSC) measurements were performed using a Discovery DSC250 (TA Instruments) under a nitrogen (N_2) atmosphere at a heating rate of 5 °C min^{-1} and the temperature range used for the measurement was −70 °C to 30 °C. Fourier Transform Infrared Spectroscopy (FTIR) of the hydrogel samples was carried out using an Equinox 55 system from Bruker in an Attenuated Total Reflection (ATR) mode. The ATR measurements were carried out in the range of 4000–370 cm^{-1} with a resolution of 2 cm^{-1} and the background spectra of air was taken as the reference before each measurement. Impedance measurements were carried out using an impedance spectrometer (Alpha high-resolution dielectric analyzer, Novocontrol Technologies GmbH) using a two-point probe method. The temperature variation study was carried out with the attached QUATRO Cryosystem 4.5. The details of the measurements can be found in the Result section. Surface morphology was studied using scanning electron microscopy (SEM, Zeiss Sigma 500 Gemini) along with energy dispersive X-ray spectroscopic analysis (EDX). The crystal structure of these samples was evaluated before and after 1 or 50 cycles through X-ray diffraction (XRD) measurements (PANalytical X'Pert PRO diffractometer) with Cu Kα radiation and a nickel filter in a Bragg–Brentano geometry. Electrochemical performance of the Zn ion battery was evaluated using a computer controlled potentiostat (SP200, BioLogic) and multichannel potentiostat VSP-3e (BioLogic) for the cyclic study. Electrochemical measurements were carried out in coin cell geometry (CR2032-type coin cells) under ambient conditions. For Zn deposition and dissolution, a symmetric cell with Zn foil (47 μm thick, 16 mm diameter) as both positive and negative electrodes was assembled with the hydrogel electrolyte. For full cell measurements, Zn foil was used as the anode and the LC/C composite was used as the cathode. The hydrogel electrolyte containing Zn salt (cut into disc shape) was used as both the electrolyte and separator. The electrodes were evaluated by cyclic voltammetry (CV) at different scan rates and galvanostatic charge discharge (GCD) by applying different charging/discharging rates (mass normalized current). The charge/discharge rates were fixed for the measurements based on the total mass of the cathode (LC and C). The charging (or discharging) capacity was obtained by dividing the product of the charging (or discharging) time and the charging (or discharging) current by the mass. Specific energy (E) and specific power (P) were calculated using $E = \frac{1}{m}\int_0^t iV\mathrm{d}t$ and $P = \frac{E}{t}$ respectively, where m is the mass, t is the time (charge or discharge), i is the current (charge or discharge) and V is the voltage. All the device data are presented based on the mass of LC active material only (excluding the mass of carbon black and Zn foil) unless otherwise mentioned.

3. Results

3.1. Thermal and structural characterization

Generally, water in hydrogels can be classified into three main types, namely, non-freezable bound water, freezable bound (intermediate) water and free water. Free water molecules have almost no interaction with the hydrogel network but they interact intimately with each other through hydrogen bonding and crystallize at about 0 °C, forming ice. Freezable bound water has some interaction with the hydrogel network and freezes below 0 °C whereas non-freezable bound water has strong interaction with the hydrogel network and does not freeze even down to −100 °C.[32,46–51] For agarose hydrogel to function effectively as an electrolyte in ZIBs, it's crucial that it maintains adequate ionic conductivity. This requires the hydrogel to contain sufficient free water, which facilitates ionic mobility within the material. However, free water will also limit device performance at lower temperatures due to the freezing of free water. There has been a lot of effort in the research

community to improve the anti-freezing properties of hydrogels and to maintain the ionic conductivity by addition of salts and use of polyol solvents such as ethylene glycol and glycerol.[32] Besides enhancing the ionic conductivity, the addition of salt to the hydrogel reduces the number of hydrogen bonding interactions between free water molecules, thus suppressing the freezing point.[52,53] In the case of polyols, hydrogen bonds between them and water molecules are stronger than the water–water hydrogen bonds. Therefore, the addition of polyols results in lowering the freezing point and helps to maintain ionic conductivity at much lower temperatures.[51,54]

In the present study the hydrogel electrolytes prepared have different water contents after drying for a given duration of time. The hydrogel was typically dried under ambient conditions at RT for 3 h. The percentage of water left in the hydrogel was determined from the initial weight and weight after drying for 3 h at RT, considering the amount of salt and glycerol present. After drying at RT for 3 h, the hydrogel consisting of 3% agarose retained 96% of its water, whereas the hydrogel consisting of 3% agarose prepared by replacing 25% of water with glycerol retained 62% of its water. Buffered hydrogel electrolytes containing 1 M Zn^{2+} with 0, 5, 10, 15, 20 and 25% glycerol had 65, 60, 56, 51, 48 and 43% water, respectively, after drying for 3 h at RT. Fig. 2a shows the effect of the addition of salt and glycerol to the 3% agarose hydrogel on the freezing point. Heating curves are considered for analysis of the hydrogel due to the presence of a large exothermic loop (artifact) of water crystallization (Fig. S1†) in the cooling curves.[55] As indicated by Fig. 2a, the crystallization of 3% agarose hydrogel starts at $T_{peak} = 5.33$ °C (blue curve); however, when 25% of water in the hydrogel is replaced by glycerol the corresponding temperature is −15.15 °C (red curve). A similar effect was observed at the freezing point when 1 M Zn salt was added (buffered) to the hydrogel (T_{peak} is −9.18 °C, pink curve). The combined effect of salt and glycerol is indicated by the curve with a T_{peak} of −26.37 °C (brown curve) and is consistent with the observations in the literature.[56,57] Fig. 2b shows the effect of glycerol addition on the freezing point, indicating a shift towards the lower temperature direction (−9.18 °C for buffered hydrogel without glycerol to −26.37 °C with 25% water replaced by glycerol). It is important to note that the endotherms in Fig. 2a and b are due to the melting of the freezable water (free and intermediate water) present in the hydrogel. The area under the heat flow curve at the melting transition is used to calculate the amount of freezable water (W_f) present in the hydrogel using $W_f(\%) = \frac{\Delta H_{Hydrogel}}{\Delta H_{Water}} \times 100$, [55,58] where $\Delta H_{hydrogel}$ and ΔH_{water} are the enthalpy of the melting transition obtained from the DSC thermogram of the hydrogel and bulk water, respectively. For the buffered hydrogels with 0, 5, 10, 15, 20 and 25% glycerol, the total amount of freezable water is determined to be 39, 23, 15, 10, 8 and 6%, respectively, and rest of the water is bound to the hydrogel network.

Importantly, the original strategy to improve the cyclability of ZIBs was to introduce glycerol to diminish the amount of free water that tends to participate in the HER side reaction. Here, the data clearly indicate that 25% glycerol in the agarose hydrogel with Zn salt almost eliminates the amount of freezable water and thus free water.

FTIR measurements were performed for the samples of buffered agarose hydrogel electrolytes containing 1 M Zn^{2+} where a portion of (wt%) the water in the hydrogel was replaced by different amounts of glycerol (0, 5, 10, 15, 20, and 25%). Fig. 3a displays the overall vibrational spectra from 4000 to 500 cm^{-1}. Different regions of the spectra are assigned to the corresponding vibration modes of interest. Vibrational bands in the frequency range of 3000–3700 cm^{-1} correspond to the OH stretching modes; while the HOH bending mode is detected at around 1640 cm^{-1}.[59,60] Bands at 2933 cm^{-1}, 2879 cm^{-1} and 1460 cm^{-1} (shoulder of 1410 cm^{-1}) are due, respectively, to asymmetric and symmetric stretching and bending of the CH_2 group of glycerol. Different vibrational bands observed in Fig. 3a (and in S2†) are consistent with the reported spectra for glycerol and agarose in the literature.[61–65] In aqueous media, the O–H stretching mode of water provides information about the hydrogen bonding [59,60] and is presented in Fig. 3b. For simplicity, the spectra have been deconvoluted into three components, around 3560 cm^{-1} (peak 1), 3428 cm^{-1} (peak 2) and 3242 cm^{-1} (peak 3).[62] The peak around 3242 cm^{-1} represents the contribution from the symmetric OH stretching, attributed to water molecules strongly bonded *via* linear hydrogen bonds into tetrahedrally coordinated water (often called quasi-crystalline water), while the 3428 cm^{-1} component represents the asymmetric, out-of-phase OH stretching

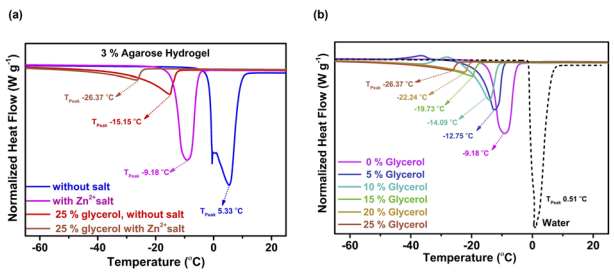

Fig. 2 DSC thermograms showing (a) the effect of salt and glycerol on the melting transitions of 3% agarose hydrogel electrolytes and (b) the effect of glycerol on the melting transitions of buffered 3% agarose hydrogel electrolyte containing 1 M Zn^{2+} salt.

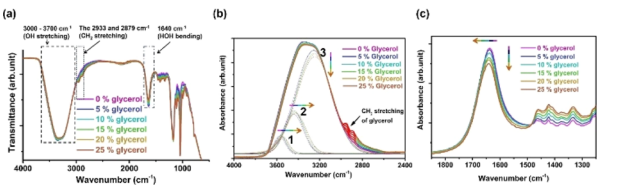

Fig. 3 (a) FTIR spectra of buffered 3% agarose hydrogel electrolyte containing 1 M Zn^{2+} with water replaced by different amounts of glycerol, (b) magnified data of the OH-stretching band along with the two deconvoluted components centered around 3250 cm^{-1} and 3460 cm^{-1}; note that the region of the spectra shown in red color (corresponding to CH_2 stretching band of glycerol) is not included for the deconvolution process and (c) magnified data of the HOH bending band.

vibrations between the nearest or next-nearest-neighbor molecules (solid-like water) and are usually characterized by non-linear and/or partially disrupted hydrogen bonds.[65,66] The vibrational band at a higher frequency, around 3560 cm^{-1}, corresponds to water molecules with a highly disturbed hydrogen bond network (liquid-like water).[62,66] As the glycerol concentration increases in the hydrogel, the overall intensity of the OH stretching mode decreases and the asymmetry in the stretching mode decreases (Fig. S2†).[67] Among the deconvoluted components, the peak around 3242 cm^{-1} shows a gradual decrease in intensity with glycerol concentration, whereas the two other components (3560 cm^{-1} and 3428 cm^{-1}) do not show major variation in intensity. Note however that both components show a slight shift towards the lower wavenumber (red shift) direction. All these observations indicate the increased hydrogen bonding between the agarose, water and glycerol molecules and lower interaction between water–water molecules.[59,62,68] Fig. 3c shows the effect of glycerol concentration in the hydrogel on the bending mode of HOH vibration (around 1640 cm^{-1}). As the glycerol percentage increases in the hydrogel, the intensity of this peak is found to decrease along with a slight shift towards higher wavenumbers. Pure glycerol does not show a significant peak in that region mainly due to the absence of an intramolecular H–O–H structure (Fig. S2†).[67] A shift in the HOH bending frequency to higher wavenumbers is indicative of increased hydrogen bonding between water and glycerol and is consistent with observations in the literature.[59,62,67,68] Overall, the FTIR studies indicate the disruption of hydrogen bonding of oxygen atoms in water with the increase in glycerol percentage in the hydrogel, while supporting hydrogen bonding between some hydrogen atoms of water molecules and oxygen atoms of glycerol molecules.[62] This is again an indication that the amount of free water decreases with the addition of glycerol, which was the proposed strategy to reduce the electrochemical side reaction in the ZIBs.

3.2. Ionic conductivity of the hydrogel electrolyte

Impedance measurements were performed using a two-point probe method with the hydrogel sandwiched between the disc electrodes (with Pt surface coating). An alternating voltage (AC voltage) of 5 mV was applied while sweeping the frequency from 10^6 Hz to 1 Hz and the measurements were carried out at RT to −30 °C . Since the measurement was performed with a 2-probe geometry, the contact resistance was determined by measuring the impedance at different thicknesses of the gel electrolyte, following the transmission line method.[69] The resistance was calculated from the Bode plot at an almost zero phase angle. The bulk ionic conductivity was calculated as $\sigma = d/(R \times A)$, where d, A and R are the distance between the electrodes, the cross section area and resistance (resistance at a near zero phase angle), respectively. The resistance used for calculations is obtained after subtracting the contact resistance. Fig. 4a shows the ionic conductivity of the 3% agarose hydrogel electrolyte in the absence and presence of glycerol at RT. Hydrogel containing 1 M Zn^{2+} shows an ionic conductivity (σ_i) of 11.6 ± 0.4 mS cm^{-1}. Buffering the hydrogel by introducing additional salts into the hydrogel resulted in a slight increase inσ_i to 12.2 ± 0.4 mS cm^{-1}. In the case of the hydrogel with 1 M Zn^{2+} salt, in which 25% of the water was replaced by glycerol, a slightly lower σ_i (10 ± 0.3 mS cm^{-1}) was observed, whereas the hydrogels with additional salt (buffering) did not show a drastic variation in σ_i (14 ± 0.4 mS cm^{-1}). Fig. 4b shows the influence of temperature on σ_i of the buffered 3% agarose hydrogel containing 1 M Zn^{2+} with 25% glycerol. As seen in the figure, the conductivity increases linearly with temperature following the Arrhenius behavior, $\sigma_i(T) = \sigma_o e^{-E_a/KT}$, where $\sigma_i(T)$ is the ionic conductivity at a given temperature, K is the Boltzmann constant, T is the absolute temperature, σ_0 is a constant related to the ionic conductivity at 0 K and E_a is the activation energy. The graph is presented as log σ_i *versus* inverse temperature and fitted with the linear equation with $R^2 = 0.99$, indicating a very good linear fit. The linear relationship observed in the polymer electrolytes indicates that there is neither phase transition in the polymer matrix nor domain formation due to the addition of salt and weak acids.[70,71] Similar temperature dependance has been reported for agar with $LiClO_4$, $KClO_4$, lactic acid and acetic acid.[70] An E_a of 34 KJ mol^{-1} was estimated from the linear fit, which is comparable to the values reported in the literature for agarose [72] and other natural polymers like gelatin [73] and starch.[74]

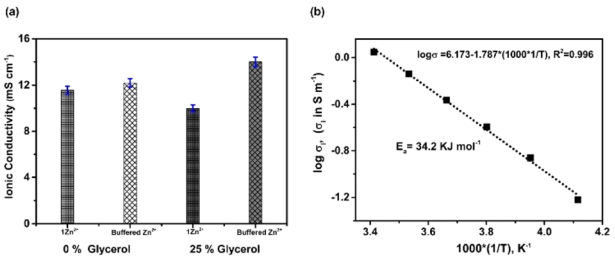

Fig. 4 (a) σ_i of the buffered and unbuffered 3% agarose hydrogel electrolytes containing 1 M Zn^{2+} in the absence and presence of glycerol and (b) Arrhenius plot showing σ_i as a function of temperature for the buffered 3% agarose hydrogel electrolyte with 1 M Zn^{2+} containing 25% glycerol.

3.3. Electrochemical compatibility of Zn and the carbon coated Ni current collector in the hydrogel electrolyte

To understand the stability of Zn and carbon coated Ni (current collector for the LC/C electrode) in the buffered 3% agarose hydrogel electrolyte containing 1 M Zn^{2+}, linear scan voltammetry (LSV) was carried out at a scan rate of 1 mV s^{-1}, with current normalized with respect to the cross-sectional area. The measurement was carried out in a three-electrode setup with Zn foil as the counter electrode, Zn wire as the reference electrode and Zn or carbon coated Ni as the working electrode. The stability is indicated by the corrosion current and the potential.[75] Fig. 5a shows the effect of glycerol in the hydrogel electrolyte on the electrochemical stability of the Zn electrode. Better stability of the Zn electrode in the hydrogel electrolyte with 25% glycerol is indicated by both a lower corrosion current (20.1 μA cm^{-2}) and a higher corrosion potential (34.5 mV *vs.* Zn/Zn^{2+}) as compared to the hydrogel without glycerol (a corrosion

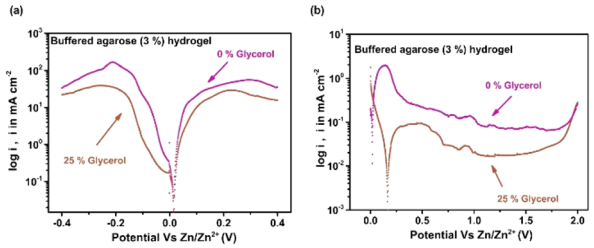

Fig. 5 (a) Stability of Zn metal and (b) carbon coated Ni current collector in the buffered 3% agarose hydrogel electrolyte containing 1 M Zn^{2+} without glycerol and in the presence of 25% glycerol (replacing the water in the hydrogel).

current of 52.1 μA cm^{-2} and a corrosion potential of 14.5 mV *vs.* Zn/Zn^{2+}). Similarly, the carbon coated Ni current collector (Fig. 5b) shows better stability in the hydrogel in the presence of glycerol with a higher corrosion potential of 166 mV *vs.* Zn/Zn^{2+} (15.5 mV *vs.* Zn/Zn^{2+}for the hydrogel without glycerol) and a lower corrosion current of 14.8 μA cm^{-2} (99.2 μA cm^{-2} for the hydrogel without glycerol). It is important to note that the LC/C electrode is coated onto the Ni-current collector that has the base coating of carbon to reduce the contact resistance. Even though Ni based materials are reported as catalysts for water electrolysis,[76,77] in the present case, the carbon coating imparts corrosion resistance to Ni in aqueous electrolytes, thus introducing larger overpotential. Therefore, the stability of the Ni current collector is influenced by the combined effect of electrolyte and the surface coating of carbon.

3.4. Electrochemical study of Zn deposition and dissolution in the hydrogel electrolyte

The effect of the hydrogel electrolyte on the Zn deposition and dissolution was further studied in a symmetric Zn/Zn cell in a coin cell geometry using Zn foil as the electrode. Details of Zn deposition (plating) and dissolution (stripping) are presented in Fig. 6 and 7. Fig. 6a shows the CV curve at a scan rate of 2 mV s^{-1} for buffered 3% agarose hydrogel electrolyte with different concentrations of glycerol and the voltage range for the measurement was −0.4 V to 0.4 V *vs.* Zn/Zn^{2+}. The CV curve shows 2 regions of slope change, and they are both found in the reduction and oxidation stages, indicating that the deposition and dissolution processes that occur in those regions are reversible. Fig. 6b indicates the variation of the peaks (slope change region) with respect to glycerol concentration in the hydrogel electrolyte. The regions of interest are indicated as R1, R2, O1 and O2 in Fig. 6a. The initial reduction of Zn^{2+} occurs on the free active Zn surface (R1); however, further deposition on the remaining surface or on the already deposited Zn layer needs additional overpotential (R2).[78,79] CV measurements at different scan rates indicate the deposition of Zn to be diffusion limited (Fig. S3a and b†). In the case of Li–metal batteries, it has been reported that the plasticizing effect of agarose and glycerol improves the ionic conductivity.[80] In the present study, glycerol in the hydrogel electrolyte has a marginal effect on the ionic conductivity (σ_i). σ_i is 12.2 ± 0.4 mS cm^{-1} and 14 ± 0.4 mS cm^{-1}

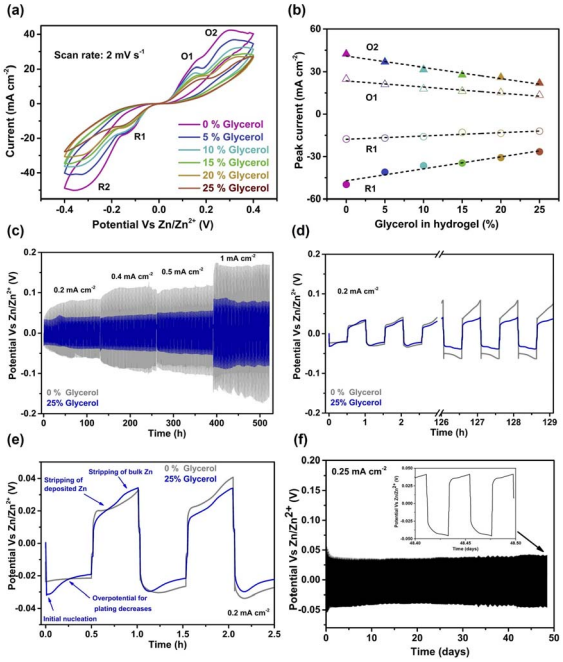

Fig. 6 (a) CV at a scan rate of 2 mV s^{-1} with the buffered 3% agarose hydrogel electrolyte containing 1 M Zn^{2+} with different amounts of glycerol, studied in a Zn/Zn symmetric system. (b) Peak current values at R1(−0.14 V *Vs* Zn/Zn^{2+}), R2 (−0.38 V *Vs* Zn/Zn^{2+}), O1(0.16 V *Vs* Zn/Zn^{2+}) and O2 (0.31 V *Vs* Zn/Zn^{2+}) for buffered 3% agarose hydrogel electrolyte with 1 M Zn^{2+} with different amounts of glycerol. (c) Galvanostatic plating and stripping of Zn in buffered 3% agarose electrolyte containing 1 M Zn^{2+} in the absence and presence of 25% glycerol at different current densities. (d) Magnified data from the initial cycle and at the end of 125 cycles of galvanostatic plating and stripping of Zn at a current density of 0.2 mA cm^{-2} showing the improved cycle performance of the hydrogel containing glycerol. (e) Different regions of the galvanostatic deposition (plating) and dissolution (stripping) of Zn in the presence and absence of glycerol. (f) Long-term cycle data of symmetric cells with a buffered 3% agarose hydrogel electrolyte containing 1 M Zn^{2+} in presence of 25% glycerol at a current density of 0.25 mA cm^{-2}, with each plating and stripping time of 30 min and the inset shows the magnified data at the end of the cycle.

for the buffered hydrogel without and with 25% glycerol, respectively. Improvement in Zn reversibility in aqueous electrolytes has been reported mainly due to the hydrogen bonding of the polyols with water molecules, thus reducing the hydrogen evolution reaction and reducing the dendritic growth.[32,81,82] It has been reported that organic molecules like glycerol can adsorb on the Zn anode surface,[83] serving as an artificial non-conductive modified layer forming a barrier to inhibit the surface migration (2D diffusion) of Zn^{2+}, resulting in a large number of small nuclei on the Zn surface, with the subsequent Zn deposition forming a dense and smooth Zn layer.[27] The efficiency of plating and stripping calculated from CV does not show any trend with the variation of glycerol concentration; however there is a clear difference in the charge efficiency in the absence of glycerol (efficiency of ∼95%) and with 25% glycerol (efficiency of 99%) (Fig. S4a†). We observe that when the glycerol content is more than 25%, the galvanostatic measurement showed a lot of noise, that is believed to be due to the beginning

of phase separation (Fig. S4b†). As the glycerol content is increased above 30%, we observe phase separation during drying of the hydrogel with the formation of water droplets on the hydrogel surface. The purpose of increasing the glycerol content in the hydrogel is to reduce free water, while simultaneously maintaining the good ionic conductivity and hydrogel stability. Hence, the hydrogel consisting of 25% glycerol is considered to be optimal for this study.

Furthermore, the reversibility of Zn deposition and dissolution was also evaluated by measuring the coulombic (charge) efficiencies in Zn||Ti asymmetrical cells using galvanostatic cycling at 1 mA cm^{-2} and a capacity of 0.5 mA h cm^{-2} using a 3% agarose buffered hydrogel electrolyte with 0 and 25% glycerol (Fig. S5†). Both electrolytes show ~90% efficiency in the first cycle. The hydrogel electrolyte containing 25% glycerol shows better reversibility reaching 98–100% charge efficiency from the 11th cycle onwards, whereas the hydrogel without glycerol shows 96–99% efficiency from the 6th cycle onwards (Fig. S5†). The CV measurements show reversibility with two regions of Zn dissolution (O1 and O2) and with the increase in glycerol concentration in the hydrogel, the peak currents decrease linearly as seen in Fig. 6b. Fig. 6c shows the effect of glycerol on the galvanostatic plating and stripping of Zn. Plating and stripping are carried out for 30 min each at different current densities, namely 0.2, 0.4, 0.5 and 1 mA cm^{-2}. At each current density, 125 cycles of plating and stripping have been carried out. Fig. 6d shows the initial and final stages of the deposition and dissolution process at a current density of 0.2 mA cm^{-2}. The increase in the overpotential for deposition and dissolution is higher for the hydrogel electrolyte without glycerol as compared to the hydrogel with 25% glycerol. The overpotential for plating varies differently for both hydrogels with 0 and 25% glycerol during the galvanostatic cycling process. The overpotential for Zn plating during the first cycle is around 24 mV for hydrogel without glycerol, whereas for the hydrogel containing 25% glycerol, the value is 32 mV. During the second cycle, the overpotential for deposition is almost the same in both hydrogels and is around 30 mV; however, from the third cycle onwards the overpotential for deposition is higher in the hydrogel without glycerol (34 mV) as compared to the hydrogel containing 25% glycerol (30 mV). The deposition overpotential keeps increasing for the hydrogel without glycerol and becomes ~62 mV at the end of 125 cycles, whereas in the case of hydrogel with 25% glycerol, the value is constant and reaches 32 mV. In addition, an abrupt initial cathodic potential drop (during the Zn deposition step) is also observed during the galvanostatic cycling that was prominent in the hydrogel without glycerol and it increases with cycling as seen in Fig. 6d. In aqueous media, Zn metal forms a thin layer of Zn oxide/hydroxide and this layer blocks hydrogen evolution.[84] These are formed and stabilized by the local increase in pH close to the Zn electrode due to the parasitic hydrogen evolution reaction, which consequently leads to a decrease in the Zn electrodeposition efficiency.[85–87] In the case of hydrogel with 25% glycerol, there is a small spike in the first cycle (that might arise due to the increased resistance to the deposition on the pristine Zn surface due to the presence of glycerol), which is found to disappear during galvanostatic cycling, resulting in a more symmetric plating and stripping profile compared to the hydrogel without glycerol.

Fig. 6e shows different regions observed in the initial stages of galvanostatic plating and stripping of Zn in the buffered hydrogel electrolyte containing 1 M Zn^{2+} with and without glycerol. For the hydrogel with 25% glycerol, initially there is an increase in the plating voltage, indicating higher overpotential activation required to start Zn plating in the presence of glycerol (as compared to the hydrogel without glycerol); however the consequent plating process on the deposited Zn is relatively easy and the potential decreases gradually. During the stripping process, two regions are observed: the initial lower potential region up to ~25 mV might be due to the stripping of the Zn layer deposited during the previous plating cycle that requires a lower overpotential (faster process), followed by the stripping of Zn from much deeper layers within the bulk Zn requiring higher overpotential (slow stripping) resulting in a lower stripping slope.[88] It is important to note that similar observations are made for the plating and stripping of Zn in the absence of glycerol; however, the initial overpotential for Zn plating is lower compared to the hydrogel with glycerol. This might be due to the adsorption of glycerol on the Zn surface that could increase the resistance to lateral Zn diffusion.[27,83] It is important to note that the zwitterionic additive, MES buffer, is also reported to modify the solvation structure of Zn^{2+} and the interface of the Zn anode, thus enabling reversible dendrite-free deposition in the Zn–MnO_2 battery system.[89] The enhancement of plating and stripping potential is more pronounced with cycling for the hydrogel without glycerol as compared to the hydrogel with 25% glycerol. Additionally, the presence of initial spikes during the plating cycle is also observed that might arise due to the increased hydrogen evolution [87] in the absence of glycerol. Fig. 6f shows the long term galvanostatic cycling of the Zn plating and stripping process, in the presence of hydrogel containing 25% glycerol at a current density of 0.25 mA cm^{-2} for 1125 cycles (~48 days) with 30 min of plating and stripping in each cycle. The inset shows the magnified data at the end of the cycling study, indicating symmetric charge–discharge behavior in the hydrogel with 25% glycerol.

3.5. Structural and morphological study of Zn deposition and dissolution in the hydrogel electrolyte

Fig. 7a and b show the XRD and morphology *via* SEM measurements, respectively, for Zn growth in buffered 3% agarose hydrogel electrolyte in the absence and presence of 25% glycerol. The measurements were performed at two different current densities, namely, 0.1 mA cm^{-2} and 1 mA cm^{-2} and the deposition and dissolution were carried out for 30 min each in a symmetric Zn/Zn cell. XRD patterns (Fig. 7a) and SEM images (Fig. 7b) of Zn electrodes after 1 cycle and 50 cycles are displayed at the mentioned current densities in the presence and absence of glycerol in the hydrogel.

As seen in Fig. 7a, the XRD patterns indicate that without glycerol, there is no significant difference between the pristine Zn and the electrodes after cycling at 0.1 mA cm^{-2}. Even though there is an increase in the relative intensity of the planes with an

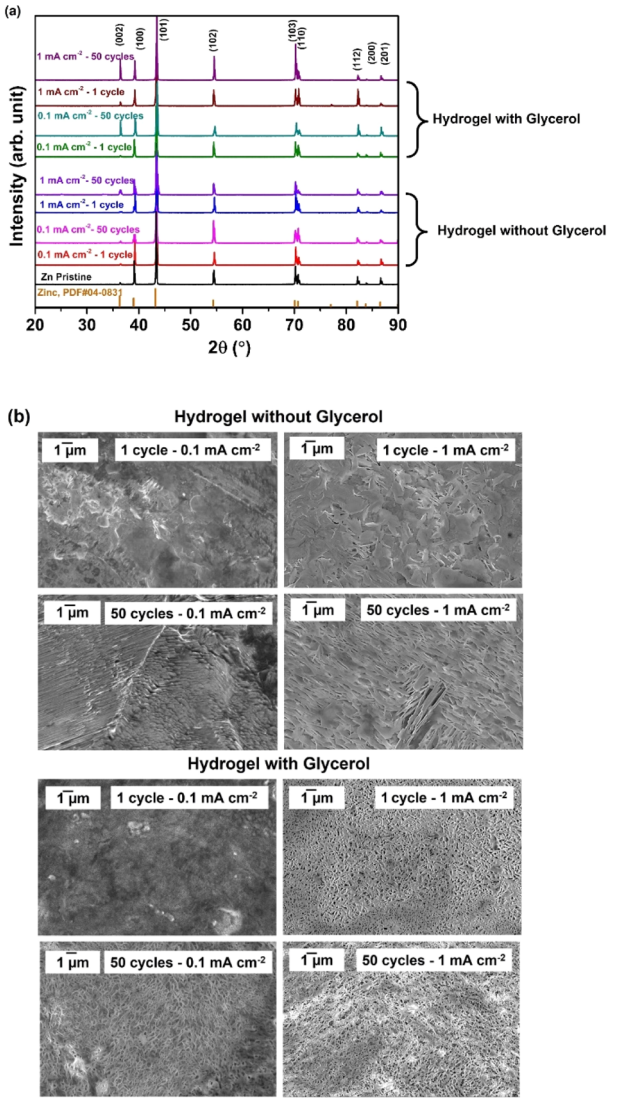

Fig. 7 (a) and (b) the XRD and SEM images respectively of Zn deposition and dissolution for 30 min each after one cycle and 50 cycles at 0.1 and 1 mA cm^{-2} current densities in buffered 3% agarose hydrogel electrolyte with 1 M Zn^{2+} in the absence and presence of glycerol (25%).

increased number of cycles and also with higher current density (1 mA cm^{-2}), the presence of all major lattice planes indicates that the deposition takes place in different crystallographic growth directions.[90,91] This is also observed in the SEM images of the Zn electrode surface shown in Fig. 7b (Zn surface for the hydrogel without glycerol). For deposition/dissolution at lower current densities (for both 1 cycle and 50 cycles), the crystallite size is larger compared to those at higher current densities (for both 1 cycle and 50 cycles). It is important to note that the hydrogel containing glycerol promotes the (002) orientation compared to the hydrogel without glycerol. This is evident from the XRD patterns at both 0.1 and 1 mA cm^{-2} current densities for 50 cycles as the relative intensity of the (002) plane is higher compared to the Zn deposition/dissolution in the absence of glycerol.

The SEM images of the Zn surface (Fig. 7b) show a morphology that is significantly different with and without glycerol in the hydrogel. The presence of glycerol leads to a highly porous interconnected cage-like network oriented parallel to the (basal plane) Zn surface and free of dendritic structures. This morphology is beneficial for the cyclic stability of the Zn ion battery/capacitor as the porous network facilitates ionic transport within the Zn electrode and create a three-dimensional electrical and ionic contact within the subsequently deposited layers.[92] As mentioned previously, the presence of glycerol inhibits the formation of dendrites by suppressing the 2D diffusion of Zn ions on the surface,[27] forming small nuclei on the surface. The correlation between the morphology and the regulated Zn deposition process has been reported in the literature, indicating that the competition between lateral and perpendicular growth governs the crystalline shapes.[79] Additionally, it depends on the current density and the degree of inhibition of lateral diffusion by the organic molecules/additives.[27,28,93] With increased constraints on lateral diffusion, dense coherent Zn deposits are formed with enhanced lateral growth,[27,79] leading to (002) oriented morphology, as observed in the hydrogel containing glycerol (Fig. 7a and b). It has been reported that, when the applied current density is small, the local current density distribution near the Zn surface becomes more uniform, which in turn slows down the dendritic growth.[28,93] Higher current densities result in the formation of dendrites, which tend to grow faster as the current density increases in neutral or mildly acidic electrolytes.[93] The current density significantly influences Zn plating in hydrogel electrolytes, where lower current densities lead to the formation of larger crystallites (laterally) in the absence of glycerol, while higher current densities promote dendritic growth. However, XRD and SEM indicate that the glycerol addition to the hydrogel results in the formation of a compact layer at both low and high current density. At high current density, the surface of Zn shows denser Zn layer formation with fine surface features.

3.6. Zn-LC/C device performance study in hydrogel electrolytes

Finally, the Zn–lignin battery was assembled with Zn foil as the anode and the LC/C composite as the cathode. The electrolyte used for the measurement was buffered 3% agarose hydrogel with 25% glycerol containing 1 M Zn^{2+}. Fig. 8a shows the CV curve of independent electrodes, with the LC electrode active at 1.2 V from the Zn redox potential. During the charging of the cell, Zn plating takes place at the anode with the oxidation of catechol to quinone at the cathode. During the discharging process, Zn stripping takes place at the anode and the reduction of quinone back to catechol takes place at the cathode. Fig. 8b shows the CV curves at different scan rates for the Zn-–lignin device. Reversible oxidation and reduction peaks at 1.36 V and 1.16 V, respectively, are associated with the two-electron/two-proton reaction ($2e^-/2H^+$) at the catechol groups of LC.[12] The inset in Fig. 8b shows the corresponding variation of peak current as a function of scan rate along with linear fitting,

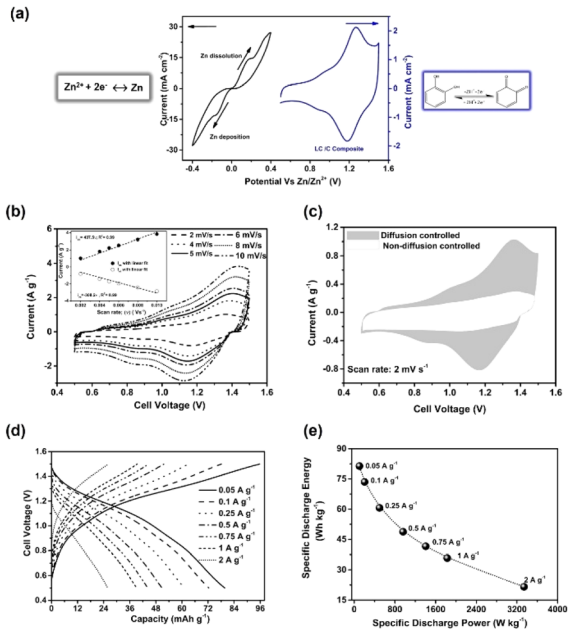

Fig. 8 Full cell configuration with Zn as the anode, the LC/C composite as the cathode and buffered 3% agarose hydrogel with 1 M Zn^{2+} and 25% glycerol as the electrolyte. (a) CV curve of the individual lignin and Zn electrodes at a scan rate of 2 mV s^{-1}. (b) CV data at different scan rates, with the inset showing the corresponding peak current *versus* scan rate variation along with the linear fit. (c) CV curve at 2 mV s^{-1} with contributions from the diffusion controlled and non-diffusion-controlled charge storage processes. (d) Galvanostatic charge and discharge plots at different charge/discharge rates. (e) Ragone plot.

indicating that the charge storage process in this range of scan rates (2–10 mV s^{-1}) is not limited by the diffusion. Furthermore, the *b* values in the power law relation between the peak current and scan rate [18] ($i = av^b$; where *i* is the peak current, *v* is the scan rate, *a* and *b* are constants) that were estimated from the slope of the log(*i*) *vs.* log(*v*) plots showed higher values in the range of 0.77–0.82 (Fig. S6†), indicating mixed charge storage kinetics in this system. The diffusion controlled (faradaic) and non-diffusion-controlled (capacitive-type) contributions were deconvoluted from the CV analysis using,[94]

$$i = k_1 v + k_2 v^{0.5}$$

where, *i* is the current, *v* is the scan rate, k_1 and k_2 are constants. The term, $k_1 v$ is the contribution from the non-diffusion limited process and $k_1 v^{0.5}$ is from the diffusion-controlled processes. The estimated values from the CV analysis at 2 mV s^{-1} show almost 43% contribution from the non-diffusion-controlled charge storage processes as shown in Fig. 8c. Bulk reaction sites from carbon (constituting 50% of the total weight of the composite cathode) and the pseudocapacitive behavior of lignin are assumed to contribute to higher non-diffusional charge storage. The galvanostatic charge and discharge plots at different charge/discharge rates are presented in Fig. 8d. The measurements were carried out with 2 cycles at each charge/discharge rate and the 2nd cycle is presented in Fig. 8d. The plots show a slight variation in the slope in the voltage region around 1.2 to 1.3 V and a maximum capacity of 79.7 mA h g_{LC}^{-1} was obtained for the 0.05 A g^{-1} charge/discharge rate. A capacity retention of 64% is observed with a 10 times increase in the charge/discharge rate from 0.05 A g^{-1} to 0.5 A g^{-1}. At higher rates, the capacity drop is faster, probably due to the diffusion limited process arising at higher rates. The Ragone plot for the device is presented in Fig. 8e. The highest specific energy of 81 W h kg_{LC}^{-1} and the highest specific power of 3338 W kg_{LC}^{-1} are obtained at charge/discharge rates of 0.05 A g^{-1} and 2A g^{-1}, respectively.

To improve the rate and cyclic stability of the device, additional salt, namely, 1 M K^+ salt (potassium mesylate), was added to the buffered 3% agarose hydrogel electrolyte containing 25% glycerol (with 1 M Zn^{2+}). For comparison, the devices were also assembled with agarose hydrogel containing 25% glycerol with 1 M Zn^{2+} and 1 M K^+, in the absence of buffering salts. Fig. 9a shows the CV comparison of the devices at a scan rate of 2 mV s^{-1}. Redox peaks are clearly seen in the CV curve of the buffered electrolyte containing 25% of glycerol with 1 M Zn^{2+} (black curve) as compared to the other two electrolytes. The

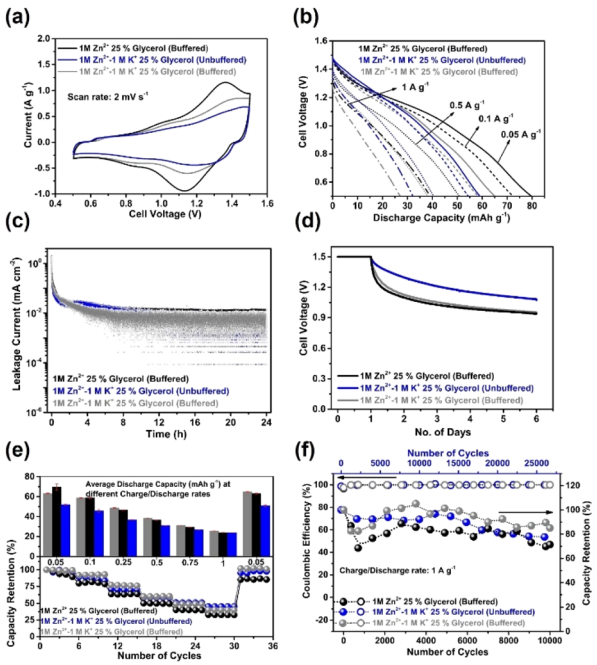

Fig. 9 Full cell data comparison with the Zn anode and LC/C composite cathode, with the electrolyte comprising a buffered 3% agarose hydrogel containing 25% glycerol with only 1 M Zn^{2+} (black data), with 1 M Zn^{2+} and 1 M K^+ (gray data) and an unbuffered 3% agarose hydrogel containing 25% glycerol with 1 M Zn^{2+} and 1 M K^+ (blue data). (a) CV data at a scan rate of 2 mV s^{-1}, (b) discharge plots at charge/discharge rates of 0.05, 0.1, 0.5 and 1 A g^{-1}, (c) leakage current measurement data, (d) self-discharge data for 5 days, (e) rate performance at charge/discharge rates of 0.05, 0.1, 0.25, 0.5, 0.75, and 1 A g^{-1} and then back to 0.05 A g^{-1} and (f) cycle performance at a 1 A g^{-1} charge/discharge rate, with open circles indicating the coulombic efficiency, and filled circles indicating capacity retention. Note that the number of cycles corresponding to the blue curve is shown on the top horizontal axis.

deconvoluted charge storage contributions from the CV curve show 47% (gray curve) and 53% (blue curve) of non-diffusion-controlled processes for the buffered hydrogel electrolyte (containing 25% glycerol with 1 M Zn^{2+} and 1 M K^{+}) and the unbuffered hydrogel electrolyte (containing 25% glycerol with 1 M Zn^{2+} and 1 M K^{+}), respectively. The deconvoluted graphs are presented in Fig. S7a.†

Fig. 9b shows the galvanostatic discharge plot at charge/discharge rates of 0.05, 0.1, 0.5 and 1 A g^{-1}. Discharge capacities of 58 mA h ${g_{LC}}^{-1}$ and 65 mA h ${g_{LC}}^{-1}$ were obtained for the unbuffered hydrogel electrolyte (blue curve) and the buffered hydrogel electrolyte (gray curve), respectively, at a charge/discharge rate of 0.05 A g^{-1} as compared to 79.7 mA h ${g_{LC}}^{-1}$ for the buffered hydrogel electrolyte with only 1 M Zn^{2+} (black curve) at the same rate. Among the three hydrogels, the highest capacity retention was observed for the device with the unbuffered hydrogel, exhibiting 70% retention when the rate was increased by 10 times from 0.05 to 0.5 A g^{-1} and 59% retention when the rate was increased from 0.1 to 1 A g^{-1}.

Fig. 9c and d show the leakage current and self-discharge data respectively, for, the devices. The leakage current was measured after charging the cell to 1.5 V and maintaining the voltage for 24 h at 1.5 V after which the open circuit voltage was measured for 120 h (5 days) to study the self-discharge behavior. A leakage current of 0.013 mA cm^{-2} was observed for the buffered hydrogel containing 25% glycerol with only 1 M Zn^{2+} (black data) whereas a leakage current of as low as 0.002 mA cm^{-2} was observed for both unbuffered (blue data) and buffered hydrogels (gray data) containing 25% glycerol with 1 M Zn^{2+} and 1 M K^{+}. During self-discharge, the cell could retain 63% and 64% of the voltage after 5 days for the devices with the buffered hydrogel containing 25% glycerol with 1 M Zn^{2+} and with 1 M Zn^{2+} and 1 M K^{+}, respectively. However, for the unbuffered hydrogel electrolyte containing 25% glycerol with 1 M Zn^{2+} and 1 M K^{+}, the voltage retention was 72% after 5 days.

Fig. 9e and f represent the rate capability of the cells and the cycle performance of the cell at a charge/discharge rate of 1 A g^{-1}, respectively. The rate performance was studied by conducting 5 cycles of galvanostatic charge/discharge at 0.05, 0.1, 0.25, 0.5, 0.75, and 1 A g^{-1} and then back to 0.05 A g^{-1}. Compared to the buffered hydrogel containing 25% glycerol with only 1 M Zn^{2+} (black data), which showed 85% retention, the rate performance of other two hydrogels (blue and gray data) is better with 98–100% retention when the charge/discharge was performed at the initial and final rate of 0.05 A g^{-1}. A capacity retention of 45% was observed for the unbuffered hydrogel electrolyte containing 25% glycerol with 1 M Zn^{2+} and 1 M K^{+} (blue data) when the rate was increased from 0.05 up to 1 A g^{-1}, whereas the retention was 40% and 33% for the buffered hydrogel containing 25% glycerol with 1 M Zn^{2+} and 1 M K^{+} (gray data) and only 1 M Zn^{2+} (black data), respectively. The cells exhibit good cycle performance with 71% capacity retention after 10 000 cycles for the buffered hydrogel electrolyte containing 25% glycerol with only 1 M Zn^{2+}(black data) whereas for the buffered electrolyte containing 25% glycerol with 1 M Zn^{2+} and 1 M K^{+} (gray data), the capacity retention was 85% after 10 000 cycles. The unbuffered hydrogel containing 25% glycerol with 1 M Zn^{2+} and 1 M K^{+} (blue data) shows 78% capacity retention after 26 000 cycles. The coulombic efficiency of all the cells is in the range of 98–100%. Generally, lignin electrodes show lower stability in acidic media, as indicated by the reduced cyclic performance due to the possible degradation of the ether bonds in modified lignin.[14] On the other hand, to achieve higher capacity and higher operating voltage, it is important to use an acidic environment.[4,11–13] Buffering the electrolyte to a higher pH is expected to decrease the capacity and increase the stability of lignin. However, high concentrations of protons may still be available in the form of the conjugated acid of the MES buffer. The protonated tertiary amine in MES is a weak acid that can participate in proton exchange reactions, resulting in higher electrode capacity as well as side reactions and degradation of lignin during cycling. The concentration of the conjugated ammonium acid in MES is 0.5 M, which at a pH of ~5.5 means that the concentration of protonated ammonium ions is 50 000 times higher than the concentration of free protons (hydronium ions). This study indicates the possibility of achieving optimized lignin performance in the Zn-ion system with a hydrogel electrolyte by the careful control of the electrolyte system, but further research is needed to understand the system completely. The Ragone plot of the cells with the Zn anode, LC/C composite cathode, and the electrolyte, buffered 3% agarose hydrogel containing 25% glycerol with only 1 M Zn^{2+} (black data), with 1 M Zn^{2+} and 1 M K^{+} (gray data), and unbuffered 3% agarose hydrogel containing 25% glycerol with 1 M Zn^{2+} and 1 M K^{+} (blue data), is presented in Fig. S7b.† A comparison of the LC/C-Zn device with other Zn-ion systems reported in the literature utilizing hydrogel electrolytes is presented in Fig. S8.† The flame test of a typical agarose hydrogel electrolyte is presented in Fig. S9,† showing the softening of the hydrogel and the absence of visible flame during burning.

4. Conclusions

The search for energy storage materials considering economic aspects, environmental friendliness and safety has driven the exploration of lignin as a potential candidate for aqueous ZIBs as it is one of the most abundant biopolymers that has the electrochemical activity perfectly fitting a Zn battery based on aqueous electrolytes. Zn–lignin batteries are among the cheapest batteries in the world, assuming a low-cost and biopolymer based electrolyte and cathode. In this work, we have considered a state-of the art lignin electrode boosted with a catechol functional group and an optimized agarose hydrogel to provide a truly green and safe battery. The buffered hydrogel electrolyte with 3% agarose containing 1 M Zn^{2+} salt in which 25% of water was replaced with glycerol to reduce the amount of free water and mitigate side reactions due to the HER competing with the plating of Zn upon charging the battery. Thermal, structural, and electrochemical characterization of the electrolyte confirms that the amount of freezing water dropped to a few percent when 25% glycerol is added in the agarose hydrogel electrolytes. Zn plating and stripping were studied in a symmetric device. The morphology and crystallographic orientation of Zn deposition indicate the importance of

glycerol in the electrolyte in reducing the formation of dendrites, improving the corrosion stability of Zn in the electrolyte and reducing hydrogen evolution, which resulted in stable cycle performance in the symmetric cell. Finally, the rate and cycle stability of the devices with the Zn anode, LC cathode and 3% agarose hydrogel electrolyte containing 25% glycerol with and without buffering are presented along with the effect of additional 1 M K^+ salt. The highest discharge capacity of 79.7 mA h $g_{LC}{}^{-1}$ was obtained at 0.05 A g^{-1} charge/discharge rate for the buffered hydrogel electrolyte containing 25% glycerol with 1 M Zn^{2+}, with 71% capacity retention after 10 000 cycles at 1 A g^{-1} charge/discharge rate. The addition of 1 M K^+ to the buffered hydrogel improves the capacity retention (85% capacity retention) after 10 000 cycles at 1 A g^{-1}, with a capacity of 65 mA h $g_{LC}{}^{-1}$ at 0.05 A g^{-1}. The hydrogel containing 25% glycerol with 1 M Zn^{2+} and 1 M K^+ in the absence of buffering shows the best cycle performance with 78% capacity retention after 26 000 cycles at 1 A g^{-1} and a capacity of 58 mA h $g_{LC}{}^{-1}$ at 0.05 A g^{-1}.

This study demonstrates, for the first time, a high performance, safe and low-cost Zn–lignin battery without fluorinated salts. This type of battery might find application in stationary batteries as it combines several unique properties: safety, a biopolymer based cathode and electrolyte and economic viability.

Data availability

Information supporting the article has been included in the ESI.† Data are available on request from the authors.

Author contributions

Conceptualization and validation: RC and UA. Hydrogel electrolyte preparation, DSC characterization, SEM, electrochemical characterization, LC/C composite and coating, writing original draft: UA. XRD and FTIR characterization: ZUK, RS and UA. Lignin modification: JB and JP. Zn salt synthesis: JB. writing and editing: UA, RC, ZUK, JB and RS. Funding and supervision: RC and MB.

Conflicts of interest

Authors declare no conflicts of interest.

Acknowledgements

This project was financed by the Swedish Electricity Storage and Balancing Centre (SESBC). The Centre is funded by the Swedish Energy Agency together with five academic and twenty-six non-academic partners. In particular, the authors acknowledge Ligna Energy for their contribution and support of the project. The authors thank the Wallenberg Wood Science Center, the Swedish Energy Agency (P52023-1), the ÅForsk foundation (22-134), and the Swedish Government Strategic Research Area in Materials Science on Functional Materials at Linköping University (Faculty Grant SFO-Mat-LiU no. 2009-00971). M. B. acknowledges the Wallenberg Scholar grant. Z. U. K. acknowledges the Swedish Research Council grant (VR 2020-04210).

References

1 B. J. Hopkins, C. N. Chervin, M. B. Sassin, J. W. Long, D. R. Rolison and J. F. Parker, *Sustainable Energy Fuels*, 2020, **4**, 3363–3369.
2 G. Li, Z. Zhao, S. Zhang, L. Sun, M. Li, J. A. Yuwono, J. Mao, J. Hao, J. Vongsvivut, L. Xing, C.-X. Zhao and Z. Guo, *Nat. Commun.*, 2023, **14**, 6526.
3 Q. Zhang, Y. Ma, Y. Lu, L. Li, F. Wan, K. Zhang and J. Chen, *Nat. Commun.*, 2020, **11**, 4463.
4 G. Milczarek and O. Inganäs, *Science*, 2012, **335**, 1468–1471.
5 F. N. Ajjan, N. Casado, T. Rębiś, A. Elfwing, N. Solin, D. Mecerreyes and O. Inganäs, *J. Mater. Chem. A*, 2016, **4**, 1838–1847.
6 F. N. Ajjan, M. J. Jafari, T. Rębiś, T. Ederth and O. Inganäs, *J. Mater. Chem. A*, 2015, **3**, 12927–12937.
7 C. Che, M. Vagin, U. Ail, V. Gueskine, J. Phopase, R. Brooke, R. Gabrielsson, M. P. Jonsson, W. C. Mak, M. Berggren and X. Crispin, *Adv. Sustainable Syst.*, 2019, **3**, 1900039.
8 S.-K. Kim, Y. K. Kim, H. Lee, S. B. Lee and H. S. Park, *ChemSusChem*, 2014, **7**, 1094–1101.
9 G. Milczarek and M. Nowicki, *Mater. Res. Bull.*, 2013, **48**, 4032–4038.
10 L. Liu, N. Solin and O. Inganäs, *RSC Adv.*, 2019, **9**, 39758–39767.
11 S. Chaleawlert-umpon, T. Berthold, X. Wang, M. Antonietti and C. Liedel, *Adv. Mater. Interfaces*, 2017, **4**, 1700698.
12 U. Ail, J. Phopase, J. Nilsson, Z. U. Khan, O. Inganäs, M. Berggren and X. Crispin, *ACS Sustain. Chem. Eng.*, 2020, **8**, 17933–17944.
13 U. Ail, J. Nilsson, M. Jansson, I. A. Buyanova, Z. Wu, E. Björk, M. Berggren and X. Crispin, *Adv. Sustainable Syst.*, 2023, **7**, 2200396.
14 U. Ail, J. Backe, M. Berggren, X. Crispin and J. Phopase, *Adv. Energy Sustainability Res.*, 2023, **4**, 2300146.
15 A. Lahiri, L. Yang, O. Höfft and F. Endres, *Mater. Adv.*, 2021, **2**, 2676–2683.
16 D. Kumar, U. Ail, Z. Wu, E. M. Björk, M. Berggren, V. Gueskine, X. Crispin and Z. Khan, *Adv. Sustainable Syst.*, 2023, **7**, 2200433.
17 D. Kumar, L. R. Franco, N. Abdou, R. Shu, A. Martinelli, C. M. Araujo, J. Gladisch, V. Gueskine, R. Crispin and Z. Khan, *Energy Environ. Mater.*, 2024, e12752.
18 N. Patil, C. de la Cruz, D. Ciurduc, A. Mavrandonakis, J. Palma and R. Marcilla, *Adv. Energy Mater.*, 2021, **11**, 2100939.
19 S. Nam, H. Seong, Y. Kim, K. Kim, C. Kim, S. Kwon and S. Park, *Chem. Eng. J.*, 2024, **497**, 154790.
20 Y. Liu, X. Lu, F. Lai, T. Liu, P. R. Shearing, I. P. Parkin, G. He and D. J. L. Brett, *Joule*, 2021, **5**, 2845–2903.
21 Y. Li, J. Yuan, Y. Qiao, H. Xu, Z. Zhang, W. Zhang, G. He and H. Chen, *Dalton Trans.*, 2023, **52**, 11780–11796.
22 B. Tang, L. Shan, S. Liang and J. Zhou, *Energy Environ. Sci.*, 2019, **12**, 3288–3304.

23 L. Ma, S. Chen, N. Li, Z. Liu, Z. Tang, J. A. Zapien, S. Chen, J. Fan and C. Zhi, *Adv. Mater.*, 2020, **32**, 1908121.
24 A. Bayaguud, Y. Fu and C. Zhu, *J. Energy Chem.*, 2022, **64**, 246–262.
25 M. A. González, R. Trócoli, I. Pavlovic, C. Barriga and F. La Mantia, *Electrochem. Commun.*, 2016, **68**, 1–4.
26 W. Hu, J. Ju, N. Deng, M. Liu, W. Liu, Y. Zhang, L. Fan, W. Kang and B. Cheng, *J. Mater. Chem. A*, 2021, **9**, 25750–25772.
27 J. Yang, B. Yin, Y. Sun, H. Pan, W. Sun, B. Jia, S. Zhang and T. Ma, *Nano-Micro Lett.*, 2022, **14**, 42.
28 Y. Zuo, K. Wang, P. Pei, M. Wei, X. Liu, Y. Xiao and P. Zhang, *Mater. Today Energy*, 2021, **20**, 100692.
29 W. Lu, C. Xie, H. Zhang and X. Li, *ChemSusChem*, 2018, **11**, 3996–4006.
30 Y. Liang, M. Qiu, P. Sun and W. Mai, *Adv. Funct. Mater.*, 2023, **33**, 2304878.
31 M. Al-Abbasi, Y. Zhao, H. He, H. Liu, H. Xia, T. Zhu, K. Wang, Z. Xu, H. Wang, W. Zhang, Y. Lai and M. Ge, *Carbon Neutralization*, 2024, **3**, 108–141.
32 S. Zhao, Y. Zuo, T. Liu, S. Zhai, Y. Dai, Z. Guo, Y. Wang, Q. He, L. Xia, C. Zhi, J. Bae, K. Wang and M. Ni, *Adv. Energy Mater.*, 2021, **11**, 2101749.
33 K. Lu, T. Jiang, H. Hu and M. Wu, *Front. Chem.*, 2020, **8**, 546728.
34 Z. Wang, H. Li, Z. Tang, Z. Liu, Z. Ruan, L. Ma, Q. Yang, D. Wang and C. Zhi, *Adv. Funct. Mater.*, 2018, **28**, 1804560.
35 E. M. Ahmed, *J. Adv. Res.*, 2015, **6**, 105–121.
36 Y. Quan, H. Ma, M. Chen, W. Zhou, Q. Tian, X. Han and J. Chen, *ACS Appl. Mater. Interfaces*, 2023, **15**, 44974–44983.
37 N. Mittal, A. Ojanguren, D. Kundu, E. Lizundia and M. Niederberger, *Small*, 2023, **19**, 2206249.
38 P. Sun, W. Liu, D. Yang, Y. Zhang, W. Xiong, S. Li, J. Chen, J. Tian and L. Zhang, *Electrochim. Acta*, 2022, **429**, 140985.
39 Z. Zheng, W. Shi, X. Zhou, X. Zhang, W. Guo, X. Shi, Y. Xiong and Y. Zhu, *iScience*, 2023, **26**, 106437.
40 V. Vandeginste and J. Wang, *Energies*, 2024, **17**, 310.
41 S. C. Baker, D. P. Kelly and J. C. Murrell, *Nature*, 1991, **350**, 627–628.
42 S. Kappenthuler, S. Olveira, J. Wehrli and S. Seeger, *J. Cleaner Prod.*, 2018, **202**, 1179–1191.
43 F. S. Mostafavi and D. Zaeim, *Int. J. Biol. Macromol.*, 2020, **159**, 1165–1176.
44 D. P. Makris and S. Lalas, *Molecules*, 2020, **25**, 5842.
45 D. J. P. Inayati and M. P. N. Matovanni, *AIP Conf. Proc.*, 2019, 2097.
46 M. Watase, K. Nishinari and T. Hatakeyama, *Food Hydrocolloids*, 1988, **2**, 427–438.
47 M. Bertasa, T. Poli, C. Riedo, V. Di Tullio, D. Capitani, N. Proietti, C. Canevali, A. Sansonetti and D. Scalarone, *Microchem. J.*, 2018, **139**, 306–314.
48 V. M. Gun'ko, I. N. Savina and S. V. Mikhalovsky, *Gels*, 2017, **3**, 37.
49 Y. Jian, S. Handschuh-Wang, J. Zhang, W. Lu, X. Zhou and T. Chen, *Mater. Horiz.*, 2021, **8**, 351–369.
50 S. V. Elgersma, M. Ha, J.-L. J. Yang, V. K. Michaelis and L. D. Unsworth, *Materials*, 2019, **12**, 832.
51 Y. Zhao, Z. Chen, F. Mo, D. Wang, Y. Guo, Z. Liu, X. Li, Q. Li, G. Liang and C. Zhi, *Advanced Science*, 2021, **8**, 2002590.
52 M. Zhu, X. Wang, H. Tang, J. Wang, Q. Hao, L. Liu, Y. Li, K. Zhang and O. G. Schmidt, *Adv. Funct. Mater.*, 2020, **30**, 1907218.
53 Y. Chen, J. Zhao and Y. Wang, *ACS Appl. Energy Mater.*, 2020, **3**, 9058–9065.
54 M. Chen, W. Zhou, A. Wang, A. Huang, J. Chen, J. Xu and C.-P. Wong, *J. Mater. Chem. A*, 2020, **8**, 6828–6841.
55 M. Vigata, C. Meinert, N. Bock, B. L. Dargaville and D. W. Hutmacher, *Biomedicines*, 2021, **9**, 574.
56 D. Zhang, Y. Liu, W. Gross, Y. Tang and J. Zheng, *Giant*, 2023, **16**, 100203.
57 Z. Zhang, Y. Gao, Y. Gao, F. Jia and G. Gao, *Chem. Eng. J.*, 2023, **452**, 139014.
58 M. A. Bag and L. M. Valenzuela, *Int. J. Mol. Sci.*, 2017, **18**, 1422.
59 T. Seki, K.-Y. Chiang, C.-C. Yu, X. Yu, M. Okuno, J. Hunger, Y. Nagata and M. Bonn, *J. Phys. Chem. Lett.*, 2020, **11**, 8459–8469.
60 Y. R. Shen and V. Ostroverkhov, *Chem. Rev.*, 2006, **106**, 1140–1154.
61 B. Zelent, N. V. Nucci and J. M. Vanderkooi, *J. Phys. Chem. A*, 2004, **108**, 11141–11150.
62 Y. Kataoka, N. Kitadai, O. Hisatomi and S. Nakashima, *Appl. Spectrosc.*, 2011, **65**, 436–441.
63 K. Prasad, G. Mehta, R. Meena and A. K. Siddhanta, *J. Appl. Polym. Sci.*, 2006, **102**, 3654–3663.
64 R. Singh, N. A. Jadhav, S. Majumder, B. Bhattacharya and P. K. Singh, *Carbohydr. Polym.*, 2013, **91**, 682–685.
65 B. Ratajska-Gadomska and W. Gadomski, *J. Chem. Phys.*, 2004, **121**, 12583–12588.
66 V. Enev, P. Sedláček, S. Jarábková, T. Velcer and M. Pekař, *Colloids Surf., A*, 2019, **575**, 1–9.
67 M. Morita, F. Matsumura, T. Shikata, Y. Ogawa, N. Kondo and K. Shiraga, *J. Phys. Chem. B*, 2022, **126**, 9871–9880.
68 H. Nakagawa and T. Oyama, *Front. Chem.*, 2019, **7**, 731.
69 T. Abbas and L. Slewa, *Int. J. Nanoelectron. Mater.*, 2015, **8**, 111–120.
70 A. C. Nwanya, C. I. Amaechi, A. E. Udounwa, R. U. Osuji, M. Maaza and F. I. Ezema, *Appl. Phys. A*, 2015, **119**, 387–396.
71 Y. Wang, *Sol. Energy Mater. Sol. Cells*, 2009, **93**, 1167–1175.
72 E. Raphael, C. O. Avellaneda, B. Manzolli and A. Pawlicka, *Electrochim. Acta*, 2010, **55**, 1455–1459.
73 C. O. Avellaneda, D. F. Vieira, A. Al-Kahlout, E. R. Leite, A. Pawlicka and M. A. Aegerter, *Electrochim. Acta*, 2007, **53**, 1648–1654.
74 R. F. M. S. Marcondes, P. S. D'Agostini, J. Ferreira, E. M. Girotto, A. Pawlicka and D. C. Dragunski, *Solid State Ionics*, 2010, **181**, 586–591.
75 S. Yang, K. Xue, J. Zhang, Y. Guo, G. Wu, C. Li, C. Xia, Y. Zhang, Y. Chen and L. Zhou, *Energy Storage Mater.*, 2023, **62**, 102929.
76 D. Li, J. Shi and C. Li, *Small*, 2018, **14**, 1704179.
77 V. Vij, S. Sultan, A. M. Harzandi, A. Meena, J. N. Tiwari, W.-G. Lee, T. Yoon and K. S. Kim, *ACS Catal.*, 2017, **7**, 7196–7225.

78 L. Oniciu and L. Mureşan, *J. Appl. Electrochem.*, 1991, **21**, 565–574.
79 J. L. Ortiz-Aparicio, Y. Meas, G. Trejo, R. Ortega, T. W. Chapman and E. Chainet, *J. Appl. Electrochem.*, 2013, **43**, 289–300.
80 P. Blin, B. Boury, A. Taguet, J. Touja, L. Monconduit and S. Patra, *Carbohydr. Polym.*, 2020, **247**, 116697.
81 R. Qin, Y. Wang, M. Zhang, Y. Wang, S. Ding, A. Song, H. Yi, L. Yang, Y. Song, Y. Cui, J. Liu, Z. Wang, S. Li, Q. Zhao and F. Pan, *Nano Energy*, 2021, **80**, 105478.
82 J. Hao, L. Yuan, C. Ye, D. Chao, K. Davey, Z. Guo and S.-Z. Qiao, *Angew. Chem., Int. Ed.*, 2021, **60**, 7366–7375.
83 Y. Zhang, M. Zhu, K. Wu, F. Yu, G. Wang, G. Xu, M. Wu, H.-K. Liu, S.-X. Dou and C. Wu, *J. Mater. Chem. A*, 2021, **9**, 4253–4261.
84 A. Bani Hashemi and F. La Mantia, *Anal. Chem.*, 2016, **88**, 7916–7920.
85 Y. Shang and D. Kundu, *Batteries Supercaps*, 2022, **5**, e202100394.
86 C. Nie, G. Wang, D. Wang, M. Wang, X. Gao, Z. Bai, N. Wang, J. Yang, Z. Xing and S. Dou, *Adv. Energy Mater.*, 2023, **13**, 2300606.
87 M. Tribbia, J. Glenneberg, G. Zampardi and F. La Mantia, *Batteries Supercaps*, 2022, **5**, e202100381.
88 Q. Li, A. Chen, D. Wang, Y. Zhao, X. Wang, X. Jin, B. Xiong and C. Zhi, *Nat. Commun.*, 2022, **13**, 3699.
89 X. Liu, B. Xu, J. Lu, J. Han, S. Deng, X. Yu, Y. An and Y. Tang, *Small*, 2024, **20**, 2307557.
90 K. O. Nayana and T. V. Venkatesha, *J. Electroanal. Chem.*, 2011, **663**, 98–107.
91 I. Kurmanbayeva, L. Rakhymbay, K. Korzhynbayeva, A. Adi, D. Batyrbekuly, A. Mentbayeva and Z. Bakenov, *Front. energy res.*, 2020, **8**, 599009.
92 A. Naveed, H. Yang, J. Yang, Y. Nuli and J. Wang, *Angew. Chem., Int. Ed.*, 2019, **58**, 2760–2764.
93 Q. Yang, G. Liang, Y. Guo, Z. Liu, B. Yan, D. Wang, Z. Huang, X. Li, J. Fan and C. Zhi, *Adv. Mater.*, 2019, **31**, 1903778.
94 T. Schoetz, L. W. Gordon, S. Ivanov, A. Bund, D. Mandler and R. J. Messinger, *Electrochim. Acta*, 2022, **412**, 140072.